Hindawi
Shock and Vibration
Volume 2020, Article ID 7426928, 11 pages
https://doi.org/10.1155/2020/7426928

Research Article

Research and Analysis of the Static Characteristics of Aerostatic Bearings with a Multihole Integrated Restrictor

Zhi-wei Lu, Jun-an Zhang, and Bo Liu

School of Mechanical and Electrical Engineering, Xi'an Technological University, Xi'an 710021, China

Correspondence should be addressed to Zhi-wei Lu; luzhiwei@xatu.edu.cn and Jun-an Zhang; zja128@163.com

Received 14 April 2019; Revised 26 July 2019; Accepted 30 January 2020; Published 29 February 2020

Academic Editor: Nawawi Chouw

In order to further study the performance of aerostatic bearing, an aerostatic bearing with a multihole integrated restrictor was proposed in this paper. Based on the physical model of aerostatic bearings, the governing equation was established, deduced discretely, and solved numerically by the finite-difference method and flow balance principle in Cartesian coordinates. The bearing capacity and stiffness of aerostatic bearings have been analyzed, and the relevant experimental research has been carried out in this paper. The results showed that the number of orifices in the integrated restrictor had a significant effect on the bearing capacity, and the maximum bearing capacity of a nine-hole integrated throttling bearing was approximately 1.9 times greater than that of a single-hole bearing. The bearing stiffness was greatly affected by the diameter of the orifices, and the optimum bearing stiffness was determined. The corresponding gas film clearance also changed accordingly.

1. Introduction

Aerostatic bearings, with a high-pressure gas supplied from an external air source passing through a restrictor of the bearing surface into the gas film clearance of the bearing, generate static pressure by means of the throttling action in the gas film clearance, leading to the function of the bearing and lubrication between the bottom of the bearing body and the working surface of the guide rail support. Because of the narrow passage that exists in some forms, the restrictor is an important pressure compensating unit for aerostatic lubrication and bearing capacity. When gas flows from the outlet and produces a pressure drop, the aerostatic film has a certain bearing capacity and stiffness. Due to their high accuracy of motion, wide speed range, small amount of friction, lack of pollution, and low heat generation, aerostatic bearings have been widely used in the aerospace industry and the IT chip manufacturing industry, as well as for the manufacturing of ultraprecision equipment and national defense application equipment in addition to other fields and applications [1–3]. With the development of precision and ultraprecision technology, higher and more urgent requirements have been proposed for the stiffness, accuracy, and stability of aerostatic bearings [4–6]. Due to the compressibility of gases, it is very difficult to improve the bearing capacity and rigidity of aerostatic bearings. Therefore, improving the bearing capacity and stiffness of aerostatic bearings is one of the difficulties and active areas in the research field of aerostatic bearings [7, 8].

To meet the development needs of ultraprecision machining and measurement, the research and development of new aerostatic bearings are extremely urgent. Researchers have focused on the analysis of the bearing structure, the control method, and the material selection of bearings to improve the stiffness, bearing capacity, and stability of aerostatic bearings [9]. Nakamura and Yoshimoto [10] studied the static characteristics of rectangular aerostatic thrust bearings and found that the stiffness of hybrid throttle bearings was greater than that of single throttle bearings. Patrick and Post Justus [11] studied the characteristics of surface throttle aerostatic bearings and pointed out the influence of the number and distribution of throttle holes and the manufacturing tolerance of throttle holes on the bearing capacity and stiffness. Fourka et al. [12] studied the relationship between the supply pressure and the relative performance of aerostatic bearings and optimized the

relevant structural parameters of aerostatic bearings by using various types of restrictors with the static characteristics of air bearings. Chen and Lin [13] designed a new type of rectangular gas-lubricated bearing with an X-shaped rigid pressure equalizing groove on the bearing surface and found that dynamic characteristic changes and the impulse response influenced the bearing performance through simulation calculations. Ma [14] designed parallel multimicrochannel aerostatic thrust bearings and studied the bearing capacity and stiffness of the bearings. The results showed that this new type of air bearing had a better bearing capacity and stiffness than traditional aerostatic bearings. To suppress the vortex air flow and reduce nanovibrations of the bearings, Chen et al. [15] proposed a novel design of aerostatic bearings with an arrayed microhole restrictor, which had uniformly distributed micron-sized holes in an arrayed pattern such that the total restriction area was the same as that of a single orifice restrictor and studied the eddy current and microvibration characteristics of aerostatic bearings with AMR by CFD analysis software. The use of porous materials could improve the performance of aerostatic bearings, leading to a good bearing capacity and stiffness and great damping and stability. However, the development and application of aerostatic bearings have been limited by the small pore size of materials, which was easily blocked during manufacturing and normal operation [16, 17].

Traditional aerostatic thrust bearings use impedance fixed restrictors such as small orifices and slits. The improvement of the load-carrying capacity and stiffness has been very limited [18, 19]. Combining the advantages and disadvantages of small orifice restrictors and porous restrictors, a new type of aerostatic bearing, the aerostatic bearing with a multihole integrated restrictor, is proposed in this paper. This new type of bearing is equipped with a restrictor on the unit area of its working surface, and numerous microholes are integrated on the restrictor. It not only overcame the problem of the porous throttling holes being easily blocked but also maintained a high bearing capacity, rigidity, stability, and other properties of the porous section. Therefore, the aerostatic bearing could be better applied to various precision and ultraprecision measuring and processing equipment. In this paper, the lubrication support mechanism of the aerostatic bearing with a multihole integrated restrictor is discussed, with a focus on the influence factors of the bearing capacity and stiffness of aerostatic bearings, which have been explored and studied based on parameters such as the number of orifices, the diameter of the orifices, and the throttled area of integrated restrictors. The performance test platform of aerostatic bearings was developed to carry out related experimental research, which provided a new method and a theoretical basis for the further study of the lubrication support mechanism of aerostatic bearings.

2. Physical Model and Governing Equation

2.1. Physical Model. To further study the static characteristics of aerostatic bearings, a new type of aerostatic bearing with a multihole integrated restrictor is proposed in this paper. Figure 1 shows its physical structure. This new type of bearing is equipped with a restrictor on the per-unit area of its working surface according to a certain rule. Numerous microholes are integrated on the restrictor and distributed along the surface of the aerostatic bearing. Microholes with diameters of 0.05–0.3 mm are arranged on each integrated restrictor. The aerostatic bearing for which the number of microholes (rounding) of each unit radius r is set to be less than $2.5r$ (radius r unit is mm) is called the aerostatic bearing with a multihole integrated restrictor in this paper.

The upper surface of the rectangular aerostatic bearing body (shown in Figure 1(a)) studied in this paper is equipped with four integrated restrictors with a unit area of radius $r = 2$ mm (shown in Figure 1(b)). Four integrated restrictors with a unit area of radius $r = 2$ mm are arranged along the surface of the aerostatic bearing according to certain rules, and at least five orifices with diameters of 0.05–0.3 mm are arranged on each integrated restrictor. The multihole integrated restrictor has one orifice in the center of the restrictor and distributes no less than five orifices with diameters of 0.05 mm–0.3 mm around the central orifice along the annular or other certain rules. The structure of the multihole integrated restrictor is shown in Figure 1(c), the material of the multihole integrated restrictor is the brass material, the microhole in the restrictor is machined by the electrical discharge machine, and the tungsten wire of 0.05 mm–0.5 mm is used as the electrode to process the microhole. The design and assembly of the multihole integrated restrictor and the aerostatic bearing body were carried out with a small interference tolerance, which was established at between 0.01 mm and 0.02 mm. The outer surface of the multihole integrated restrictor was machined with a shallow groove, and the outer surface of the multihole integrated restrictor was coated with high-strength glue. When assembling, high-strength glue entered into shallow grooves and played the role of sealing and fixing. In Figure 1(c), A1, A2, A3, and A4, respectively, are the length sizes of the structural characteristic parameters of the multihole integrated restrictor; Ød1, Ød2, Ød3, Ød4, and Ød, respectively, are the diameter sizes of the structural characteristic parameters of the multihole integrated restrictor.

For the convenience of writing and understanding, the name of each type of multihole integrated restrictor is defined as $n \times d$, where n denotes the number of microsmall orifices on each restrictor and d denotes the diameter of the microsmall orifices. For example, 5×0.2 indicates five microsmall orifices with a diameter of 0.2 mm on the multihole integrated restrictor.

The aerostatic bearing with a multihole integrated restrictor is a kind of hydrostatic bearing. It uses high-pressure air with a certain pressure as a moving lubricating medium. Figure 2 shows its working principle sketch.

The high-pressure air with a certain pressure is supplied from external air source equipment. After the supply air is purified by air-pneumatic triple parts, the air is regulated and stabilized. Then, it enters multiple air passage 6 in the aerostatic bearing body 4 through the air inlet 5. To ensure

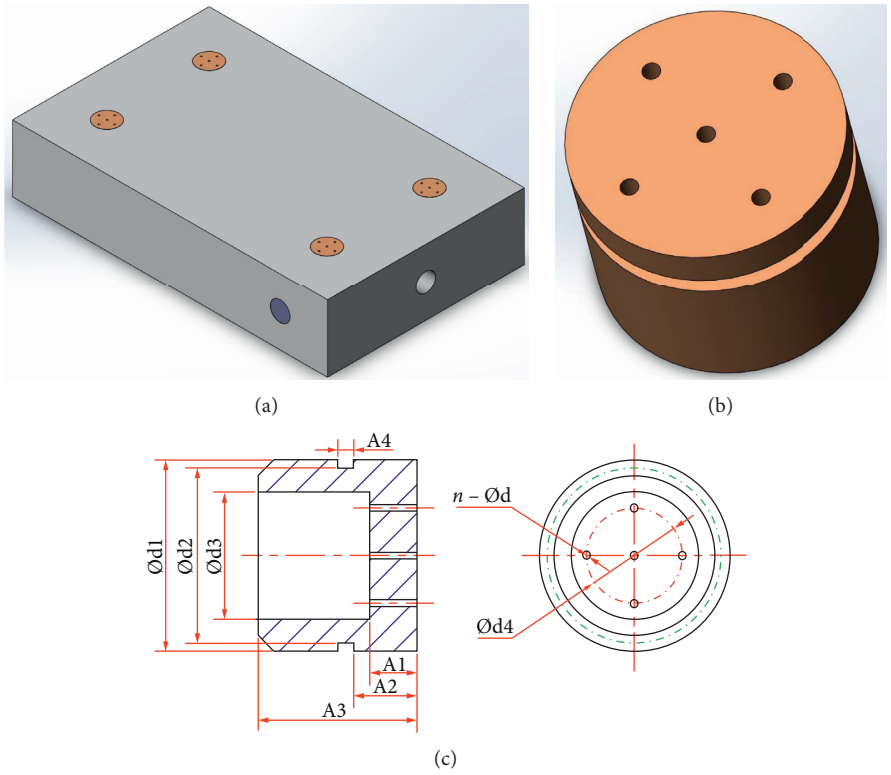

Figure 1: Schematic diagram of the physical model of aerostatic bearings with multihole integrated restrictor: (a) aerostatic bearing body; (b) multihole integrated restrictor; (c) structural chart of multihole integrated restrictor.

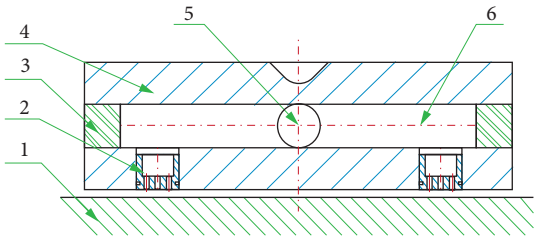

Figure 2: Schematic diagram of the working principle of the aerostatic bearing with a multihole integrated restrictor.

that each air passage 6 is running through each other and preventing air leakage, numerous plungers 3 are installed in the process hole. Afterwards, the air enters the many integrated restrictors 2 for throttling. Finally, the air enters between two moving parts (aerostatic bearing body 4 and guide rail bearing face part 1) to produce a certain pressure support and lubrication film to support and balance the external load. When aerostatic bearings work, there is always high-pressure lubricating air between the two moving parts, leading to no direct contact between them. Therefore, aerostatic bearings have remarkable characteristics such as no friction and wear, no creeping at low speed, a high accuracy of motion, good damping characteristics, and a good homogenization effect of the gas film.

2.2. Governing Equation of Gas Lubrication. The fluid motion proposed in the film clearance of aerostatic bearings with a multihole integrated restrictor meets three physical laws: mass conservation, momentum conservation, and energy conservation. Therefore, the basic equations for fluid control include the relative continuity equation, the momentum equation, and the energy equation, and the Cartesian tensor expressions are given by formulas (1)–(3), respectively:

$$\frac{\partial \rho}{\partial t} + \frac{\partial \rho u_j}{\partial x_j} = 0, \tag{1}$$

$$\frac{\partial \rho u_i}{\partial t} + \frac{\partial \rho u_j u_i}{\partial x_j} = \rho f_i - \frac{\partial p}{\partial x_i} + \frac{\partial \tau_{ji}}{\partial x_j}, \tag{2}$$

$$\frac{\partial \rho E}{\partial t} + \frac{\partial \rho u_j E}{\partial x_j} = \rho f_j u_j - \frac{\partial p u_j}{\partial x_j} + \frac{\partial u_j \tau_{ij}}{\partial x_i} - \frac{\partial}{\partial x_i}\left(k \frac{\partial T}{\partial x_j}\right) + S', \tag{3}$$

where t is the time, ρ is the density, u_j is the velocity component in the j direction in Cartesian coordinates, f_i is the volumetric force component acting in the j direction in Cartesian coordinates, p is the pressure, τ_{ij} is the element of the viscous stress tensor (component), the subscript i is the normal direction of the action surface, the subscript j is the projection direction of the force, E is the total internal energy of the unit mass fluid, k is the thermal conductivity, T is the temperature, and S' is the volume heat source term.

In the two-dimensional low-speed state, the lubricating fluid for aerostatic bearings with a multihole integrated

restrictor is investigated. Its relative sliding speed between the aerostatic bearing and the plane of the guide rail is very small compared with the flow rate generated by the gas pressure. Then, the lubricating fluid is assumed to be a two-dimensional steady compressible fluid. The static performance of the rectangular aerostatic bearings with a multihole integrated restrictor is investigated in this paper. To ensure mesh division and numerical convergence and stability, the aerostatic bearings are numerically calculated in the Cartesian coordinate system. By deducing and simplifying equations (1)–(3), the air lubrication control equation (4) is obtained in its Cartesian coordinates:

$$\frac{\partial^2 p^2}{\partial x^2} + \frac{\partial^2 p^2}{\partial y^2} + \frac{3}{h}\frac{\partial h}{\partial x}\frac{\partial p^2}{\partial x} + \frac{3}{h}\frac{\partial h}{\partial y}\frac{\partial p^2}{\partial y} = 0, \tag{4}$$

where h is the gap film clearance, x is the abscissa in Cartesian coordinates, and y is the ordinate in Cartesian coordinates.

According to the theory of fluid lubrication, it can be concluded that the fluid flow in the gas film clearance of the bearing should be balanced with the fluid flow at the outlet of each orifice of the bearing, and the equation of flow balance (5) should be satisfied:

$$Q_{\text{in}} = Q_{\text{out}}. \tag{5}$$

In formula (5), Q_{in} is the flow rate into the gas film clearance through the orifice, and its expression is expressed by the following formula:

$$Q_{\text{in}} = AC_0\Psi\frac{p_s}{\sqrt{RT_0}}. \tag{6}$$

Among them, in equation (6),

$$\Psi = \left(\frac{2\kappa}{\kappa-1}\left(\left(\frac{p_0}{p_s}\right)^{(2/\kappa)} - \left(\frac{p_0}{p_s}\right)^{(\kappa+1/\kappa)}\right)\right)^{(1/2)}, \quad \frac{p_0}{p_s} \geq \left(\frac{2}{\kappa+1}\right)^{(\kappa/\kappa-1)}.$$

$$\Psi = \left(\frac{2\kappa}{\kappa+1}\left(\frac{2}{\kappa+1}\right)^{(2/\kappa-1)}\right)^{(1/2)}, \quad \frac{p_0}{p_s} < \left(\frac{2}{\kappa+1}\right)^{(\kappa/\kappa-1)}, \tag{7}$$

where A is the area of the throttle orifice, C_0 is the flow coefficient of the nozzle, p_0 is the outlet pressure of the throttle orifice, p_s is the pressure of the external supply, T_0 is the temperature of the supply gas, and κ is the adiabatic coefficient.

Q_{out} is the flow rate of the outflow film gap into the surrounding environment. Formula (8) is the calculation formula of the rectangular aerostatic bearings with a multihole integrated restrictor.

$$Q_{\text{out}} = \frac{h^3}{12\mu}\int_0^L \left\{\left|\frac{\partial p}{\partial y}\right|_{y=0} + \left|\frac{\partial p}{\partial y}\right|_{y=B}\right\} \mathrm{d}x\gamma_a + \frac{h^3}{12\mu}\int_0^B \left\{\left|\frac{\partial p}{\partial x}\right|_{x=0} + \left|\frac{\partial p}{\partial x}\right|_{x=L}\right\} \mathrm{d}y\gamma_a, \tag{8}$$

where γ_a is the density of the gas at normal temperature and pressure, μ is the dynamic viscosity of the gas, L is the length of the bearing in the x direction, and B is the length of the bearing in the y direction.

2.3. Calculation Formula of Bearing Capacity and Stiffness. According to the governing equation of gas lubrication (4) and the flow balance equation (5), the pressure distribution in the gas film clearance is solved jointly. The bearing capacity W and the stiffness K of the aerostatic bearings with a multihole integrated restrictor can be obtained from the bearing capacity formula (9) and the stiffness formula (10):

$$\text{Bearing capacity } (W) = \int_0^B \int_0^L [p - p_a]\mathrm{d}x\mathrm{d}y, \tag{9}$$

$$\text{Stiffness } (K) = \frac{\mathrm{d}W}{\mathrm{d}h}. \tag{10}$$

3. Numerical Calculation

3.1. Discrete Governing Equation of Gas Lubrication. The governing equation (4) is discretized by the finite difference method, and the numerical accuracy of the second-order central finite difference method is used to solve the problem in this paper.

The node of the x direction is expressed by i, and the node of the y direction is expressed by j, meaning each node can be represented by (i, j) in Cartesian coordinates. If f is approximately equal to p^2, then equation (4) will be discretized by the second-order center difference and merged into formula (11):

$$f_{i,j} = \frac{1}{B_{i,j}}\left(\frac{f_{i+1,j} + f_{i-1,j}}{(\Delta x)^2} + \frac{f_{i,j+1} + f_{i,j-1}}{(\Delta y)^2} + \frac{3}{h_{i,j}}\frac{h_{i+1,j} - h_{i-1,j}}{2\Delta x}\frac{f_{i+1,j} - f_{i-1,j}}{2\Delta x} + \frac{3}{h_{i,j}}\frac{h_{i,j+1} - h_{i,j-1}}{2\Delta y}\frac{f_{i,j+1} - f_{i,j-1}}{2\Delta y}\right), \tag{11}$$

where $B_{i,j} = ((2/\Delta x)^2 + (2/\Delta y)^2)$.

3.2. Boundary Conditions. The aerostatic bearings are rectangular aerostatic bearings with a multihole integrated restrictor in this paper. The bearings are connected with the atmosphere around them, and the bearings are symmetrical. Therefore, a quarter of the OACD part of the bearings is taken as the research object. As shown in Figure 3, the boundary conditions are as follows:

(1) When $x = 0$, $p = p_a$; when $x = L/2$, $(\partial p/\partial x) = 0$.

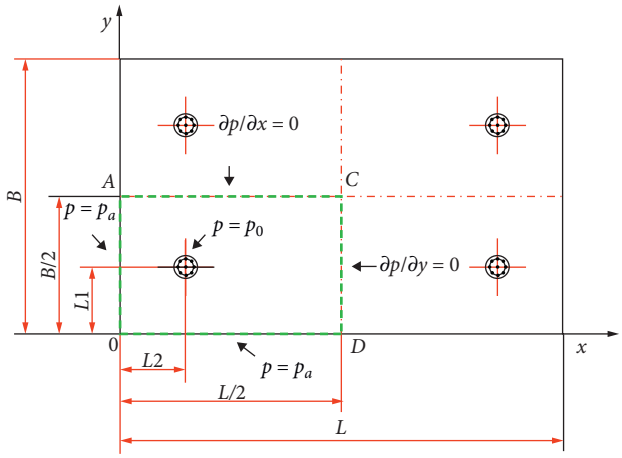

FIGURE 3: Schematic diagram of the boundary conditions in the computational domain.

(2) When $y = 0$, $p = p_a$; when $y = B/2$, $(\partial p/\partial y) = 0$.

(3) When $x = L1/2$ and $y = B2/2$, no matter how many microholes are installed on the unit area integrated restrictor, the outlet pressure of all microholes in the integrated restrictor of the unit area is the same; that is, $p = p_0$.

Here, p_a is the ambient atmospheric pressure and p_0 is the outlet pressure of the throttling hole.

3.3. Calculation Process. The finite-difference numerical iterative solution calculation is performed on the discrete control equation (11) by the superrelaxation iterative method, and the pressure distribution and performance parameters of the bearing film can be obtained in this paper. When solving the governing equation (11) numerically, it is necessary to set the values of the gas film bearing clearance h and the pressure P_0 at the outlet of each orifice to obtain the pressure distribution. However, the values of P_0 and h must satisfy the flow balance requirement of equation (5) at the same time. The arbitrarily set values of P_0 and h generally cannot satisfy both equations (5) and (11) at the same time and need to be adjusted by numerical calculation. The supply pressure p_s of the aerostatic bearings is a fixed value. If p_0 is larger, p_s–p_0 will be smaller, leading to a smaller Q_{in}. When h is set to be constant, if p_0 is larger, the overall pressure distribution will increase, leading to larger Q_{out}. Therefore, it is possible to determine whether to increase or decrease the set value of Q_{out} according to the comparison of the sizes of Q_{in} and Q_{out}, thus satisfying both equations (5) and (11) at the same time. Figure 4 shows the calculation diagram of the aerostatic bearings with a multihole integrated restrictor.

4. Results and Discussion

4.1. Pressure Distribution. The rectangular multihole integrated restrictor aerostatic bearing with a length $L = 80$ mm and a width $B = 50$ mm is selected as the research object. Figure 1 shows the physical model. By using the difference expression of the governing equation (11), the boundary conditions, and the flow chart of bearing performance calculations, the numerical calculation is solved by the overrelaxation iterative method. Because the bearings investigated are symmetrical, one-fourth of them is taken as the research objects. The number of grids in the x direction is $N = 160$, and the number of grids in the y direction is $M = 100$. Thus, the spacing of the grid in the x direction and the y direction is 0.25 mm, basically ensuring that each microthrottle hole on the unit area throttle is on the computational grid point. The supply gas is assumed to be a normal temperature gas for a supply pressure $P_s = 0.5$ MPa, an external environmental pressure $P_a = 0.1$ MPa, a gas constant of air $R = 287$ J/(kg·K), an absolute temperature $T = 288$ K, an adiabatic index of the air $\kappa = 1.4$, an aerodynamic viscosity coefficient $\mu = 1.883 \times 10^{-5}$ N·s/m^2, a gas flow coefficient of the nozzle $c_0 = 0.85$, a density of the air $\rho = 1.226$ kg/m^2, and an iterative convergence accuracy $\varepsilon = 1 \times 10^{-6}$. Based on a different number of orifices, different diameters of the orifices, and the same throttled area of the integrated restrictor, the influence factors of the bearing capacity W and stiffness K of the aerostatic bearings with a multihole integrated restrictor are analyzed, and the influence factors of the static performance of the aerostatic bearings with a multihole integrated restrictor and the optimum matching rule of the performance parameters are explored.

Five orifices with a diameter $d = 0.2$ mm are distributed on the integrated restrictor with a unit area of radius $r = 2$ mm. The gas film pressure distribution of the aerostatic bearings is numerically solved at gas film clearances h of 10 μm, 20 μm, 30 μm, and 40 μm. Figure 5 shows the numerical results of the gas film pressure distribution.

It can be seen from Figures 5(a)–5(d) that the distribution of gas film pressure p is symmetrically distributed under different gap film clearances h. This is mainly because the physical model of the rectangular aerostatic bearing with a multihole integrated restrictor is a symmetrical model, and the multihole integrated restrictor is uniformly distributed on its working surface.

With the increase in the gas film clearance h from 10 μm to 40 μm, the pressure distribution p in the gas film also changes significantly and appears to show a decreasing trend. The peak of the pressure p at the outlet of the orifice also decreases from 0.499 MPa to 0.260 MPa. It can be concluded that, with the increase in the gas film clearance h, the gas film pressure distribution p of the aerostatic bearings and the comprehensive bearing capacity W also decrease.

4.2. Static Characteristics of the Aerostatic Bearing with a Multihole Integrated Restrictor

4.2.1. Static Characteristic Analysis under the Different Numbers of Orifices. The influence factors of the static characteristics of the aerostatic bearings are analyzed and studied for different numbers of orifices in the per-unit restrictor on the aerostatic bearing with a multihole integrated restrictor. With $n = 1$, $n = 3$, $n = 5$, $n = 7$, $n = 9$, $n = 13$, and $n = 17$ and with the other parameters of the integrated

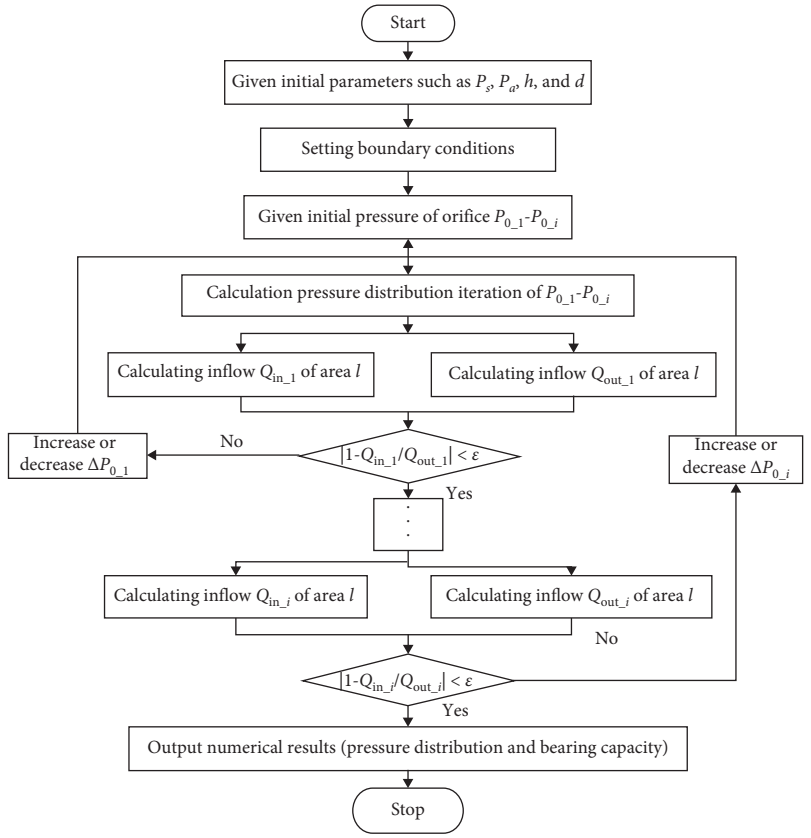

Figure 4: Calculation diagram.

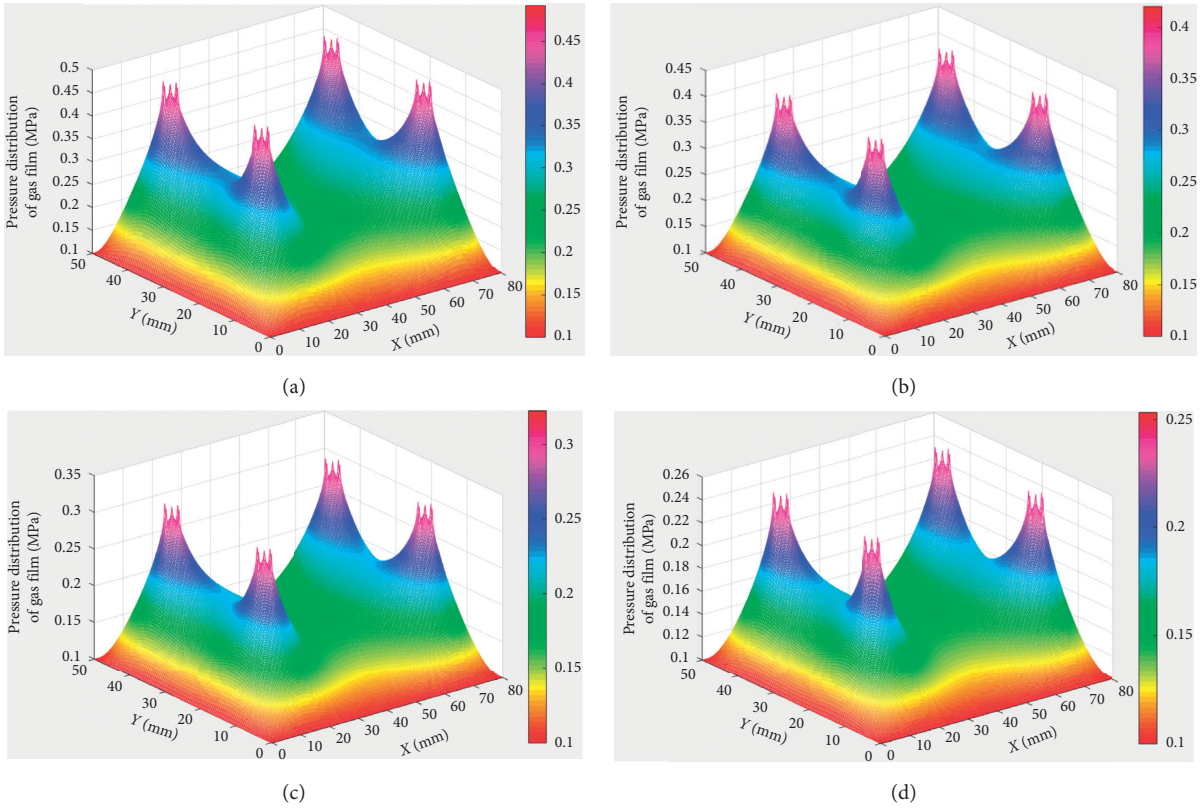

Figure 5: Diagram of gas film pressure distribution: (a) $h = 10\,\mu$m; (b) $h = 20\,\mu$m; (c) $h = 30\,\mu$m; (d) $h = 40\,\mu$m.

restrictor unchanged, the effects of the number of orifices n on the bearing capacity W and stiffness K of the aerostatic bearing with a diameter $d = 0.2$ mm are analyzed. Figures 6 and 7 show the numerical results.

As seen from Figure 6, with the increase in the gap film clearance h, the bearing capacity W of the aerostatic bearings decreases. With the increase in the number of orifices n and the same film clearance h, the bearing capacity W increases. The maximum bearing capacity of a nine-hole integrated throttle bearing is approximately 1.9 times that of a single-hole bearing, which shows that the number of orifices of the integrated restrictor has a significant effect on the bearing capacity. However, with the increase in the number of orifices n to a certain extent, the bearing capacity W increases slowly. By increasing the number of orifices n, the bearing capacity of the bearing can be improved. However, when the number of orifices n reaches a certain value, the bearing capacity of the bearing is not obviously increased by increasing the number of orifices n.

It can be seen from Figure 7 that, with the increase in the gap film clearance h, the bearing stiffness K of the aerostatic bearings increases gradually. However, when the bearing stiffness K increases to a certain extent, the bearing stiffness K decreases gradually with the increase in the gap film clearance h. Under a certain gap film clearance h, the optimum bearing stiffness K exists for various types of aerostatic bearings. With the increase in the number of orifices n, the optimum bearing stiffness K increases. However, with the increase in the number of orifices n to a certain extent, the optimum bearing stiffness K decreases. With the number of orifices n, the optimum bearing stiffness K increases, and the gap film clearance h corresponding to the optimum bearing stiffness K also gradually increases.

4.2.2. Static Characteristic Analysis under the Different Diameter Orifices. The static characteristics of the aerostatic bearings are analyzed and studied for the different diameters of orifices in the per-unit area throttle on the aerostatic bearing with a multihole integrated restrictor in this paper. When the other parameters of the integrated restrictor are unchanged, the influence of the throttle orifice diameter d on the bearing capacity W and bearing stiffness K is analyzed for the aerostatic bearing, with $n = 5$ for the number of orifices of the integrated restrictor. For $d = 0.01$ mm, $d = 0.05$ mm, $d = 0.1$ mm, $d = 0.15$ mm, $d = 0.2$ mm, $d = 0.25$ mm, and $d = 0.3$ mm, the numerical results are shown in Figures 8 and 9.

It can be seen from Figure 8 that the bearing capacity W of the aerostatic bearings decreases with the increase in the gap film clearance h. Nevertheless, the smaller the diameters d of the orifices is, the more obvious the decreasing trend is. The diameters d of the orifices have little effect on the maximum bearing capacity W of the aerostatic bearing. However, with the increase in the gap film clearance h, under the same condition of the gap film clearance h, the bearing capacity W increases gradually with the increase in the diameters d of the orifices.

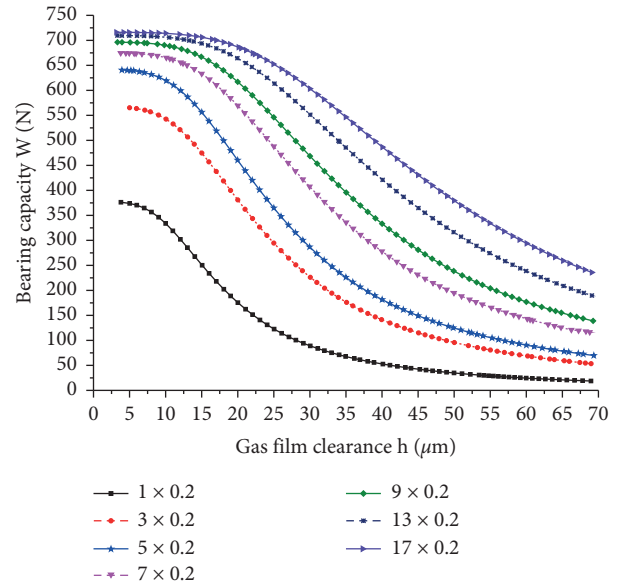

Figure 6: Curve of influence of the number of orifices n on the bearing capacity.

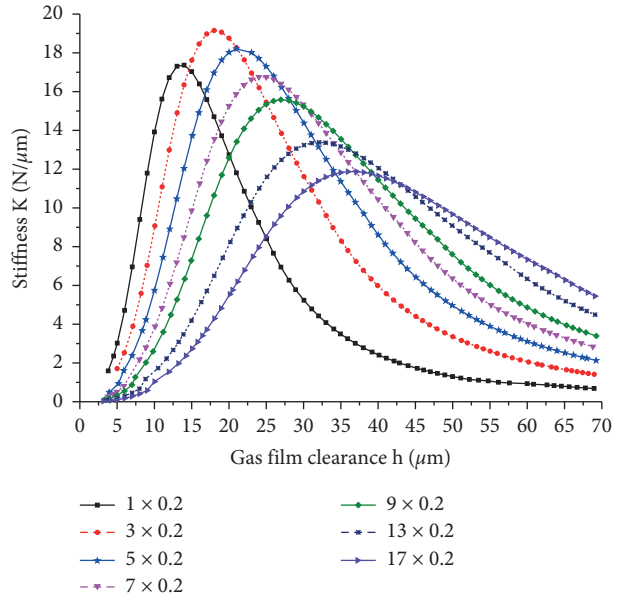

Figure 7: Curve of influence of the number of orifices n on the bearing stiffness.

It can be seen from Figure 9 that, with the change in the gap film clearance h, under a certain gap film clearance h, the aerostatic bearing has an optimal bearing stiffness K. With the decrease in the diameters d of the orifices, the optimum stiffness K increases gradually. The optimum bearing stiffness K decreases with the decrease in the diameters d of the orifices, and the gap film clearance h, corresponding to the optimum bearing stiffness K, decreases gradually.

The diameters d of the orifices have a significant influence on the bearing stiffness K of the aerostatic bearing. Especially when it is smaller, the influence of diameters d of the orifices is more obvious. The bearing stiffness K of the

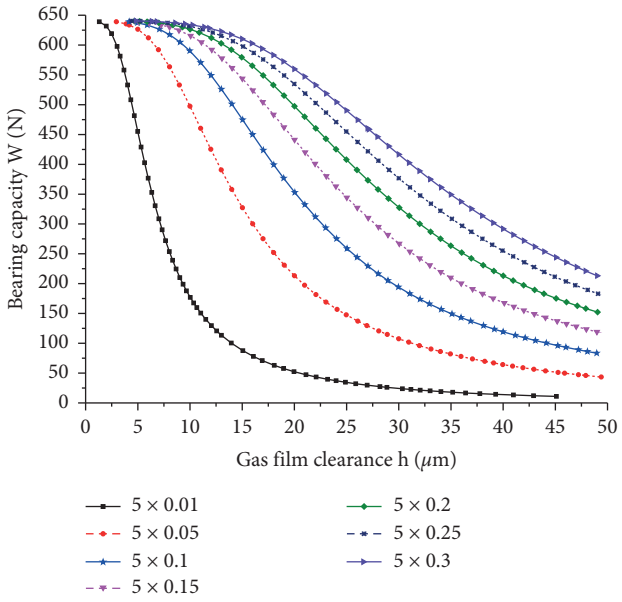

Figure 8: Curve of influence of the diameters d of the orifices on the bearing capacity.

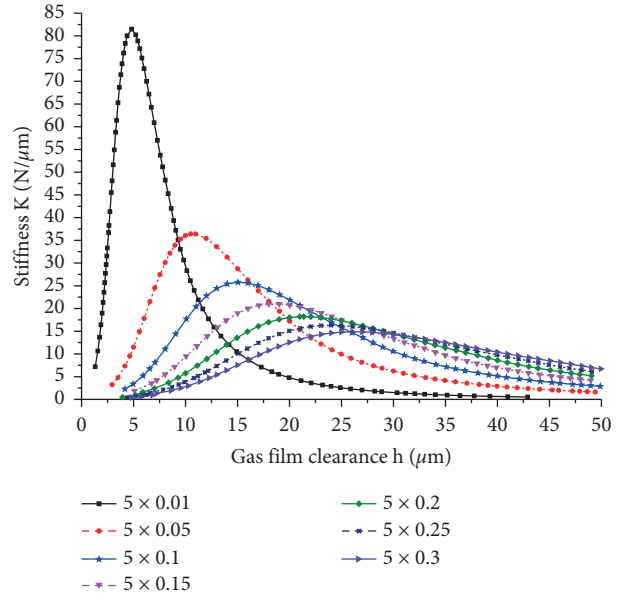

Figure 9: Curve of influence of the diameters d of the orifices on the bearing stiffness.

aerostatic bearings can be increased by reducing the diameters d of the orifices. Nevertheless, the minimum limit size of the diameters d of the orifices is limited by the machining capability. When the diameters d of the orifices is less than 0.05 mm, the traditional machining process reaches its limit. Therefore, other factors should be considered comprehensively to improve the comprehensive static characteristics of the aerostatic bearings.

4.2.3. Static Characteristic Analysis under the Same Throttled Area of Integrated Restrictor. When the restrictor orifice of a multihole integrated restrictor has the same throttle area S, the static characteristics of the aerostatic bearing are analyzed and studied for the number and diameter of the throttle orifice. When the other parameters of the integrated restrictor remain unchanged, the comprehensive effects of the number and diameter of the throttle orifice are analyzed based on the performance of the aerostatic bearings with an integrated restrictor, a unit area of radius $r = 2$ mm, and a throttle area of the orifices $S = n\pi dh = 0.8\pi h$ mm^2. For $nd = 1 \times 0.8$, $nd = 2 \times 0.4$, $nd = 4 \times 0.2$, $nd = 8 \times 0.1$, and $nd = 16 \times 0.05$, under aerostatic bearings with $S = 0.8\pi h \cdot$mm^2, the effects on the bearing capacity W and the bearing stiffness K are analyzed and studied. The numerical results are shown in Figures 10 and 11.

As seen from Figure 10, the bearing capacity W of the aerostatic bearings decreases with the increase in the gap film clearance h. When the gap film clearance h is less than 35 μm, under the same gap film clearance h for the various types of aerostatic bearings with the same throttle orifice area S, the bearing capacity W gradually increases with the increase in the number of orifices n and the decrease in the diameters d of the orifices. However, when the gap film clearance h is greater than 35 μm and has the same throttle orifice area S, the curves of the bearing capacity W for various types of aerostatic bearings tend to coincide. The number of orifices n and the diameters d of the orifices have little effect on the bearing capacity W.

It can be seen from Figure 11 that, with the increase in the gap film clearance h, the values of the bearing stiffness K of various types of aerostatic bearings, which have the same throttle orifice area S, are also gradually increased. When the bearing stiffness K increases to a certain extent, it gradually decreases. Under a certain gap film clearance h, the optimum bearing stiffness K is found. With the increase in the number of orifices n and the decrease in the diameters d of the orifices, the optimum bearing stiffness K gradually increases, and the gap film clearance h corresponding to the optimum bearing stiffness K gradually decreases.

5. Experimental

5.1. Experimental Device. On the basis of theoretical numerical calculations and an analysis of the aerostatic bearings with a multihole integrated restrictor, further experimental research is carried out. According to the structure and performance parameters of the aerostatic bearings, a performance test platform for aerostatic bearings is developed, which mainly tests and analyzes the bearing capacity, bearing stiffness, gap film clearance, and other related parameters of aerostatic bearings.

Figure 12 shows the overall schematic diagram of the performance test platform for aerostatic bearings. The mechanical and testing system is installed in the mouth-shaped granite frame 1, and the mouth-shaped granite frame 1 is placed on the granite base 15 to provide vibration isolation 14 between the mouth-shaped granite frame 1 and the granite base 15. An installation bracket 6, connection bracket 7, and connection plate 8 are installed on the left side of the mouth-shaped granite frame 1, leaving installation

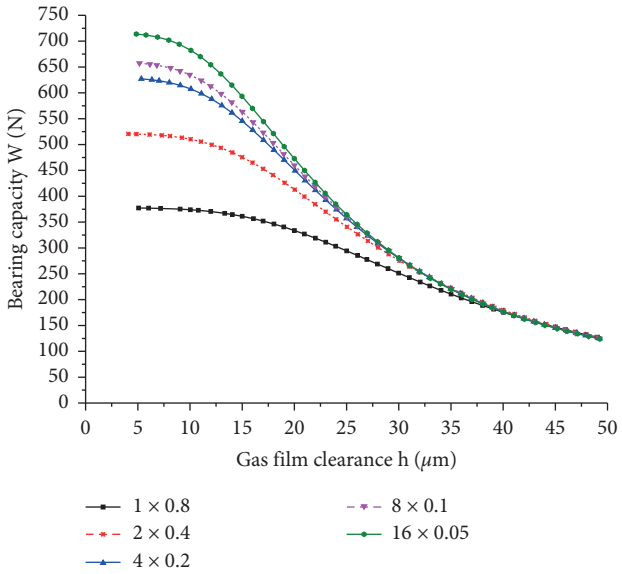

Figure 10: Curve of influence of the same throttled area on the bearing capacity.

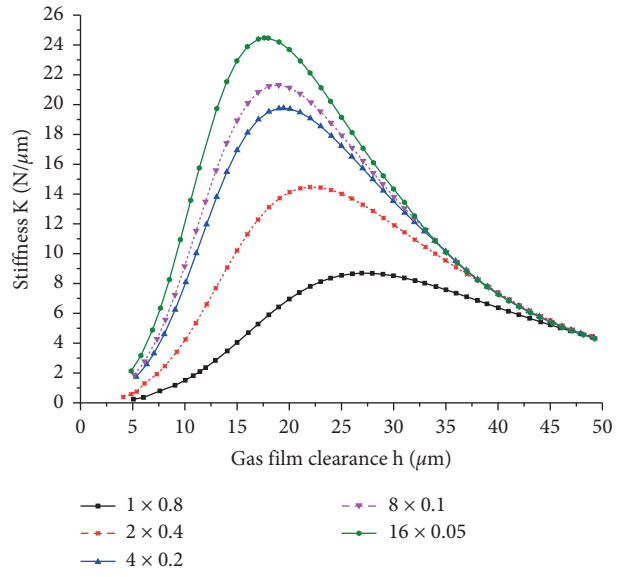

Figure 11: Curve of influence of the same throttled area on the bearing stiffness.

interfaces for subsequent dynamic testing. A loading cylinder 4, static force rod 5, pressure measuring disc 11, and loading platform 13 are connected in turn along the vertical centerline of the mouth-shaped granite frame 1. Loading cylinder 4 is fixed by a cylinder block 2, top wire 3, and mouth-shaped frame 1. Cylinder 4 loads continuous loading force F on the tested bearing 10 through a static force bar 5, and a steel ball 9 is set between the static force bar 5 and the tested bearing 10 to prevent eccentricity of the loading force F. The tested bearing 10 is placed on the pressure measuring disc 11, and the pressure hole is set on the pressure measuring disc 11 according to certain rules to test the pressure distribution of the tested bearing 10. The pressure measuring

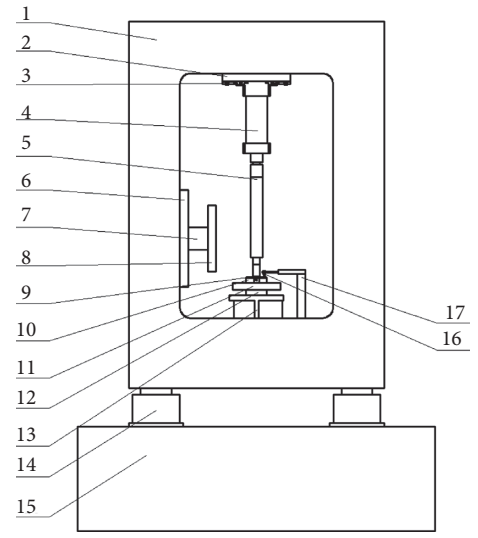

Figure 12: Schematic diagram of the overall structure for the test platform.

disc 11 is placed on the bearing platform 13. To test the external load force F of the bearing 10, static force sensors 12 are installed between the pressure testing plate 11 and the bearing platform 13, and the bearing platform 13 is installed on the mouth-shaped granite frame 1. To test the gap film clearance h of the tested bearing 10, a support bracket 17 is installed in the mouth-shaped granite frame 1 for clamping and adjusting a displacement sensor 16.

By adjusting the pressure of the inlet and outlet ports of the loading cylinder 4, continuous loading of the tested bearing 10 can be realized. According to the test requirements, by adjusting the inlet pressure of the tested bearing 10, load testing is carried out through the static force sensor 12, and the gas film clearance h of the tested bearing 10 is measured by the displacement sensor 16. The related parameters of the air supply pressure, bearing capacity, gas film clearance, and bearing stiffness of other related parameters of the aerostatic bearings can be tested separately. Figure 13 shows the physical device diagram of the test platform.

The gas film clearance of the tested bearing specimens in the test platform is tested by a DGS-6C digital inductance micrometer and a DGC-8 ZG/D inductance displacement sensor probe, and the measurement range is 100 μm with a resolution of 0.1 μm. The bearing capacity of the tested bearing specimens is measured by an LH-S10D force sensor with a resolution of 0.1 N and a force range of 0–1000 N.

5.2. Experimental Results. Three kinds of rectangular aerostatic bearings with a length $L = 80$ mm and a width $B = 50$ mm are selected as test specimens in this paper. The diameter d of the orifices of the multihole integrated restrictors is $d = 0.2$ mm, and the number of orifices of the multihole integrated restrictors is $n = 1$, $n = 5$, and $n = 9$. The external supply pressure P_s is 0.5 MPa, the external environment pressure P_a is 0.1 MPa, and the absolute temperature T is 288 K. The numerical calculation and experimental test results of the aerostatic bearings with a multihole

Figure 13: Diagram of the physical device for the test platform.

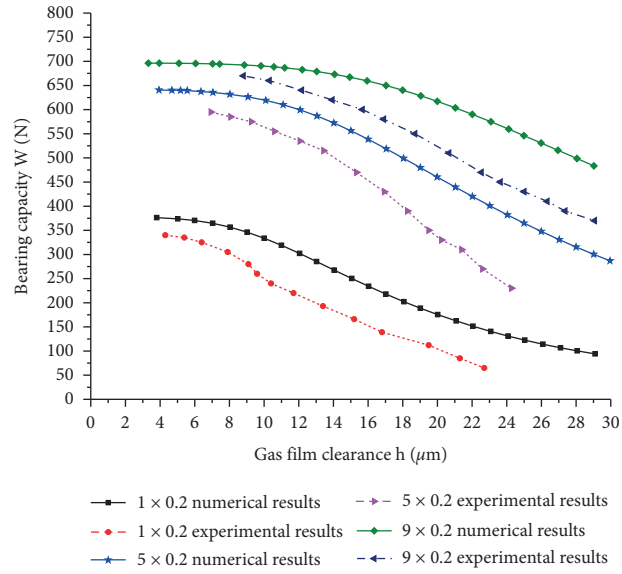

Figure 14: Curves of theoretical and experimental results of bearing capacity.

integrated throttle bearing are compared and analyzed. Figure 14 shows the numerical calculations and experimental test results.

As seen from Figure 14, the bearing capacity W of the aerostatic bearings with three different structures gradually decreases with the increase in the gap film clearance h. Under the same gap film clearance h, the bearing capacity of the aerostatic bearings with a number of orifices $n = 9$ is the largest, and that of the aerostatic bearings with a number of orifices $n = 1$ is the smallest. The maximum bearing capacity of the nine-hole integrated throttle bearing is approximately 1.9 times that of the single-hole bearing, which shows that the number of orifices of the integrated restrictor has a significant effect on the bearing capacity. With the increase in the gap film clearance h, the difference of the bearing capacity W of three different aerostatic bearings with a multihole integrated restrictor tends to decrease. The experimental results are consistent with the general trend of the numerical results, which also verifies the feasibility and correctness of the numerical results and the numerical calculation method.

In Figure 14, the overall results of the numerical calculation results and the experimental test results are consistent. However, there are some differences between the calculation results and the experimental test results of the aerostatic bearing. The bearing capacity W of the experimental test is generally lower than that of the numerical calculation. The main reasons for this phenomenon are as follows:

(1) Although the mathematical model considers many major influencing factors, there are still some factors that have less impact and are ignored, leading to higher numerical results.

(2) The flow balance equation used for numerical calculations should adopt an adiabatic model at the outlet of the restrictor, and the nozzle flow coefficient C_0 should be a variable parameter coefficient rather than a given empirical constant.

(3) The accuracy and consistency of the data acquisition sensor of the experimental test platform and the influence of the external environment on the experimental test should be considered.

(4) It is assumed that the working plane of the bearings is an ideal one in the numerical calculations, but due to limitations of the actual grinding and polishing processing level, the working surface Ra of the actual bearing specimen is approximately 0.1 μm, the flatness is approximately 0.9 μm, the supporting surface Ra of the pressure measuring disc is approximately 0.1 μm, and the flatness is approximately 1 μm. All of these parameters are high in the center and low in the circumference, which results in the difference of the sealing effect of the bearing and the test of the film clearance of the bearing.

(5) The roundness of the multiple orifices on the bearing throttle and the consistency of the diameters of the orifices are not easy to strictly guarantee in actual processing, which will also cause some differences between the numerical calculations and the experimental results.

6. Conclusion

A new type of aerostatic bearings with a multihole integrated restrictor was proposed in this paper. The influence of several performance parameters for the multihole integrated restrictor on the bearing capacity and stiffness of aerostatic bearings is explored and studied, and the related experimental verification work was performed in this paper. From the results, we made the following conclusions:

(1) With the increase in the number of orifices, the bearing capacity of the aerostatic bearings with a multihole integrated restrictor increases. The number of orifices of the integrated restrictor has a significant effect on the bearing capacity. The maximum bearing capacity of a nine-hole integrated throttle bearing was approximately 1.9 times greater than that of a single-hole bearing, and the bearing capacity of the aerostatic bearings with a multihole integrated restrictor is obviously better than that of the aerostatic bearing with a single-hole restrictor.

(2) Under a certain film clearance, all kinds of aerostatic bearings have their optimum bearing stiffness. With the increase in the throttle orifice number, the optimum bearing stiffness first increases and then decreases. The diameter of the throttle orifice has an obvious influence on the bearing stiffness. With the increase in the number of orifices and the decrease in the diameters of the orifices, for the same throttle orifice area, the optimum bearing stiffness of the bearings gradually increases.

(3) Through numerical calculations and experimental tests, the experimental results are in good agreement with the numerical results, which verifies the feasibility and accuracy of the numerical calculations and the numerical method. This study further enriches the theory of and experimental research on the lubrication support of aerostatic bearings and provides a new idea and theoretical basis for further improving the bearing capacity and stiffness of aerostatic bearings.

Data Availability

The data used to support the findings of this study are available from the corresponding author upon request

Conflicts of Interest

The authors declare that they have no conflicts of interest.

Acknowledgments

This research was supported by the National Natural Science Foundation of China (51705390), Science and Technology Project of Weiyang District (201838), Key Laboratory Project of Shaanxi Province Education Department (19JS033), and Xi'an Technological University School-Level Fluid Lubrication Technology Research and Innovation Team.

References

[1] J. Zhang, D. Zou, N. Ta, and Z. Rao, "Numerical research of pressure depression in aerostatic thrust bearing with inherent orifice," *Tribology International*, vol. 123, pp. 385–396, 2018.

[2] Z. Xiao-long, Z. Jun-an, D. Hao, F. Zhou, and L. Jun-ning, "Numerical simulation and experimental study on the gas-solid coupling of the aerostatic thrust bearing with elastic equalizing pressure groove," *Shock and Vibration*, vol. 2017, Article ID 5091452, 11 pages, 2017.

[3] S. Yoshimoto, M. Yamamoto, and K. Toda, "Numerical calculations of pressure distribution in the bearing clearance of circular aerostatic thrust bearings with a single air supply inlet," *Journal of Tribology*, vol. 129, no. 2, pp. 384–390, 2007.

[4] Q. Gao, L. Lu, W. Chen, and G. Wang, "Influence of air-induced vibration of aerostatic bearing on the machined surface quality in ultra-precision flycutting," *Proceedings of the Institution of Mechanical Engineers, Part J: Journal of Engineering Tribology*, vol. 232, no. 2, pp. 117–125, 2018.

[5] C. Schenk, S. Buschmann, S. Risse, R. Eberhardt, and A. Tünnermann, "Comparison between flat aerostatic gas-bearing pads with orifice and porous feedings at high-vacuum conditions," *Precision Engineering*, vol. 32, no. 4, pp. 319–328, 2008.

[6] H. Cui, "Static and dynamic characteristics of aerostatic bearing based on numerical simulation," *Journal of Mechanical Engineering*, vol. 52, no. 9, pp. 116–121, 2016.

[7] Y. Li, X. Wan, and X. Li, "Microvibration suppression of an aerostatic thrust bearing adopting flow field disturbance structure," *Advances in Mechanical Engineering*, vol. 9, no. 9, pp. 1–9, 2017.

[8] Z.-w Lu, F.-j Ma, B. Liu, and Z. Jun-an, "Research on dynamic characteristics of aerostatic thrust bearings based on perturbation method," *Acta Armamentarii*, vol. 37, no. 1, pp. 149–154, 2016.

[9] Y. Li and K. Zhou, "Flow-difference feedback iteration method for aerostatic bearings," *Journal of Tsinghua University (Science and Technology)*, vol. 57, no. 9, pp. 980–985, 2017.

[10] T. Nakamura and S. Yoshimoto, "Static tilt characteristics of aerostatic rectangular double-pad thrust bearings with compound restrictors," *Tribology International*, vol. 29, no. 2, pp. 145–152, 1996.

[11] K. Y.-B. Patrick and B. Post Justus, "A tolerancing procedure for inherently compensated rectangular aerostatic thrust bearing," *Tribology International*, vol. 33, pp. 581–585, 2000.

[12] M. Fourka, Y. Tian, and M. Bonis, "Prediction of the stability of air thrust bearings by numerical, analytical and experimental methods," *Wear*, vol. 198, no. 1-2, pp. 1–6, 1996.

[13] M. F. Chen and Y. T. Lin, "Static behavior and dynamic stability analysis of grooved rectangular aerostatic thrust bearings by modified resistance network method," *Tribology International*, vol. 35, no. 5, pp. 329–338, 2002.

[14] W. Ma, "Study on loading characteristic of parallel micro-channel compensated aerostatic thrust bearing," *Northeast Forestry University*, vol. 12, pp. 51–66, 2013.

[15] X. Chen, H. Chen, J. Zhu, and W. Jiang, "Vortex suppression and nano-vibration reduction of aerostatic bearings by arrayed microhole restrictors," *Journal of Vibration and Control*, vol. 23, no. 5, pp. 842–852, 2017.

[16] Y. B. P. Kwan and J. Corbett, "Porous aerostatic bearings-an updated review," *Wear*, vol. 222, no. 2, pp. 69–73, 1998.

[17] C. Wu, "Theoretical and experimental research of porous air bearings," *Tianjin University*, vol. 5, pp. 2–7, 2012.

[18] D. Chen, Y. Bian, S. Zhou et al., "Influence factor Analysis for gas fluctuation of aerostatic guideway," *Journal of Mechanical Engineering*, vol. 50, no. 15, pp. 97–103, 2014.

[19] N. Mondal, R. Saha, and D. Sanyal, "Modeling and performance analysis of aerostatic bearings for lifting heavy payload," *Procedia Engineering*, vol. 90, pp. 123–128, 2014.